

Comparison of image quality between step-and-shoot and continuous bed motion techniques in whole-body ^{18}F -fluorodeoxyglucose positron emission tomography with the same acquisition duration

Shozo Yamashita¹ · Haruki Yamamoto¹ · Tetsu Nakaichi¹ · Tatsuya Yoneyama² · Kunihiro Yokoyama³

Received: 13 June 2017 / Accepted: 6 August 2017 / Published online: 16 August 2017
© The Japanese Society of Nuclear Medicine 2017

Abstract

Objective This study aimed to compare the qualities of whole-body positron emission tomography (PET) images acquired by the step-and-shoot (SS) and continuous bed motion (CBM) techniques with approximately the same acquisition duration, through phantom and clinical studies. **Methods** A body phantom with 10–37 mm spheres was filled with ^{18}F -fluorodeoxyglucose (FDG) solution at a sphere-to-background radioactivity ratio of 4:1 and acquired by both techniques. Reconstructed images were evaluated by visual assessment, percentages of contrast ($\%Q_H$) and background variability ($\%N$) in accordance with the Japanese guideline for oncology FDG-PET/computed tomography (CT). To evaluate the variability of the standardized uptake value (SUV), the coefficient of variation (CV) for both maximum SUV and peak SUV was examined. Both the SUV values were additionally compared with those of standard images acquired for 30 min,

and their accuracy was evaluated by the %difference ($\%Diff$). In the clinical study, whole-body ^{18}F -FDG PET/CT images of 60 patients acquired by both techniques were compared for liver signal-to-noise ratio (SNR_{liver}), CV at end planes, and both SUV values.

Results In the phantom study, the visual assessment and $\%Q_H$ values of the two techniques did not differ from each other. However, the $\%N$ values of the CBM technique were significantly higher than those of the SS technique. Additionally, the CV and $\%Diff$ for both SUV values in the CBM images tended to be slightly higher than those in SS images. In the clinical study, the SNR_{liver} values of CBM images were significantly lower than those of SS images, although the CV at the end planes in CBM images was significantly lower than those in SS images. In the Bland–Altman analysis for both SUV values, the mean differences were close to 0, and most lesions exhibited SUVs within the limits of agreement.

Conclusions The CBM technique exhibited slightly lesser uniformity in the center plane than the SS technique. Additionally, in the phantom study, the CV and $\%Diff$ of SUV values in CBM images tended to be slightly higher than those of SS images. However, since these differences were subtle, they might be negligible in clinical settings.

Keywords Positron emission tomography (PET) · Step-and-shoot (SS) · Continuous bed motion (CBM) · Whole body · Acquisition duration

✉ Shozo Yamashita
y.shozo57@gmail.com

¹ Division of Radiology, Public Central Hospital of Matto Ishikawa, 3-8 Kuramitsu, Hakusan 924-8588, Japan

² Division of Thyroid, Public Central Hospital of Matto Ishikawa, 3-8 Kuramitsu, Hakusan 924-8588, Japan

³ PET Imaging Center, Public Central Hospital of Matto Ishikawa, 3-8 Kuramitsu, Hakusan 924-8588, Japan

Introduction

Positron emission tomography (PET) images are conventionally acquired by the step-and-shoot (SS) technique, which involves repetitive static acquisition and covers the

required scan range by overlapping of regions. This overlapping might lead to image artifacts and degradation of axial uniformity due to under-sampling in the axial direction [1–4]. In this mode, since the scan range cannot be arbitrarily created because of the variations in individual bed positions, operators sometimes add a redundant scan range in the axial field-of-view (FOV) during the protocol setup. This addition of a redundant range results in increased total scan time and radiation exposure in computed tomography (CT) protocols matching the axial scan range of PET [5].

The continuous bed motion (CBM) method has been implemented as an alternative PET acquisition technique [1–9]. Similar to spiral CT, the CBM technique involves continuous movement of the scan table during acquisition without a stationary state. The total scan times are determined by the velocity of table motion and scan range in the axial FOV instead of, as in the SS mode, acquisition time per bed and number of bed positions. The CBM technique does not entail additional time for moving the scan table from one bed to another. Moreover, it allows for a flexible protocol setup, and operators can arbitrarily select the exact axial scan range without the necessity of adding redundant regions. Relative to the SS technique, the CBM technique produces better uniform axial sensitivity without loss of the spatial resolution, because an additional acquisition plane is added on both sides of the axial FOV in order to obtain a uniform profile throughout the scan range; moreover, owing to the continuous acquisition mode, the CBM technique does not involve overlapping of regions [1–3, 6]. This technique, which is used not only for PET/CT but also for PET/magnetic resonance imaging, has been reported to be feasible in clinical settings [10, 11].

Previous studies have reported slight differences in image quality between the SS and CBM techniques. Brasse et al. [4] reported that the CBM technique provides better hot contrast than the SS technique, which leads to improved lesion detectability in clinical studies. Several studies have demonstrated that the CBM technique provides improved uniformity of reconstructed images because of its uniform axial sensitivity profile [1–4, 6–8, 11–13]. Although most previous studies have reported that the CBM technique provides slightly better image quality than the SS technique, one study has demonstrated that the CBM technique produces slightly higher background variability than the SS technique in a National Electrical Manufacturers Association (NEMA) phantom [14]. Therefore, the differences between the two techniques are not yet to be clearly established. In this study, we performed comparative assessment of image quality in whole-body images acquired by both techniques with approximately the same acquisition duration, through phantom and clinical studies.

Materials and methods

Phantom study

Phantom preparation

The phantom study was performed using a NEMA International Electrotechnical Commission body phantom (Data Spectrum Corp., Hillsborough, NC, USA), which consisted of a torso cavity, a removable lung insert, and six spheres with inner diameters of 10, 13, 17, 22, 28, and 37 mm. The phantom was filled with ^{18}F -fluorodeoxyglucose (FDG) solution at a sphere-to-background radioactivity ratio of 4:1. The background radioactivity was decided referring to the Japanese guideline for oncology FDG-PET/CT [15]. At our institution, ^{18}F -FDG is injected with radioactivity of 4.4 kBq/g, and SS or CBM techniques were performed at approximately 60 min after injection (physical decay to 68.5%). Assuming that the percentage of injected radioactivity excreted in the urine is 20%, and the percentage of the adipose tissue is 27% of the total body volume, the radioactivity at the start of data acquisition is estimated to be 3.3 kBq/mL ($4.4 \text{ kBq/g} \times 1 \text{ g/mL} \times 0.685 \times 0.8/0.73 = 3.3$). The background radioactivity was, therefore, set to 3.3 kBq/mL. For acquisition of standard images, background radioactivity was set to 2.65 kBq/mL.

Data acquisition and image reconstruction

All PET/CT images were acquired with the Biograph mCT Flow 20-4R (Siemens Medical Solutions USA, Inc., Knoxville, USA). The PET detector comprised an array of 32,448 lutetium oxyorthosilicate crystals of size $4 \times 4 \times 20 \text{ mm}^3$. The scanner comprised four 842-mm-diameter detector rings with 48 detector blocks per ring (a total of 192 blocks), covering an axial FOV of 216 mm and a transaxial FOV of 700 mm. The coincidence timing window and time-of-flight (TOF) system timing resolution were 4.1 ns and 540 ps, respectively.

The phantom was scanned using the CBM and SS techniques. Image acquisition with the SS technique was performed with eight bed positions that simulated the whole-body scan range in clinical settings. Hot spheres were placed at the center of the axial FOV, which corresponded to the center of the overlapped region between bed positions 4 and 5. The acquisition time was set to 1.5 min/bed.

The CBM protocol was designed to match the axial FOV of the SS technique. The table speed was set to 1.5 mm/s to correspond with the total scan time of the SS

technique; CBM acquisition times that corresponded with the scan ranges of bed positions 7, 8 and 9 were 10 min 50 s, 12 min 13 s and 13 min 37 s, respectively. The phantom was firstly scanned by the SS technique, followed immediately by the CBM technique (SS → CBM). The order was reversed (CBM → SS) to account for the radioactivity decay between the two scans. Image acquisition was performed 5 times per order of scanning. To obtain standard images, the phantom was scanned for 30 min with one bed position, and the process was repeated 5 times.

Images were reconstructed using the 3D ordered subset expectation maximization (OSEM) and TOF–OSEM algorithms with iteration-subset combinations of 3–24 and 3–21, respectively. A 5-mm full-width at half-maximum Gaussian filter was used for reconstruction. Slice thickness and matrix size were set at 3.0 mm and 200×200 , respectively. Attenuation correction was performed using a 20-slice CT scanner. Scatter correction was performed in the relative mode. The CT images were reconstructed using the sinogram-affirmed iterative reconstruction algorithm with the following scanning parameters: tube voltage, 120 kV; quality reference mAs, 40; rotation time, 0.5 s; pitch, 1.0; slice thickness, 3.0 mm; transaxial FOV, 780 mm; and matrix size, 512×512 .

Data analysis

Visual analysis was performed using syngo. via VB10B (Siemens Healthcare GmbH, Erlangen, Germany). The hot spheres were evaluated by three experts including a certified PET physician from the Japanese Society of Nuclear Medicine and two certified PET technologists from the Japan Board of Nuclear Medicine Technology. Evaluations were performed using those slices where the spheres were most prominent. The images were displayed in an inverse grayscale, with a standardized uptake range of 0–4. The hot spheres were visually graded as follows: identifiable, 2; visualized, but similar hot spots were observed elsewhere, 1; and not visualized, 0. Spheres with visual scores ≥ 1.5 were adjudged to be detectable. The visual analysis was performed based on the Japanese guideline [15].

Physical analysis was performed using the PET Quality Control Tool (PETquact) ver. 2.02.03 (Nihon Medi-Physics Co., Ltd., Tokyo, Japan) and syngo. via VB10B (Siemens Healthcare GmbH, Erlangen, Germany). The mean activity ($C_{H,j-mm}$) of six spheres (j) was measured using a region of interest (ROI) of the same diameter. The background was measured using 12 ROIs of the same diameter, with six spheres in the same slice. Further, 12 ROIs were placed in four additional slices (± 1 and ± 2 cm of the upper and lower sides of the slice, respectively). The average values

of 60 ROIs ($C_{B60,j-mm}$) were calculated, and %contrast ($\%Q_{H,j-mm}$) was calculated using the following formula:

$$\%Q_{H,j-mm} = \frac{C_{H,j-mm}/C_{B60,j-mm} - 1}{4 - 1} \times 100(\%).$$

Additionally, %background variability ($\%N_{j-mm}$) was calculated using the following formula:

$$\%N_{j-mm} = \frac{SD_{j-mm}}{C_{B60,j-mm}} \times 100(\%),$$

where SD_{j-mm} is the standard deviation (SD) of the background ROI values for each diameter of spheres.

To evaluate the variability of the standardized uptake value (SUV), coefficient of variation (CV) for both maximum SUV (SUV_{max}) and peak SUV (SUV_{peak}) were examined in both SS and CBM images. The SUV_{peak} was measured using a spherical volume of interest of 1-cm^3 with a 12-mm diameter positioned so as to maximize the enclosed average activity. The CV was calculated by the ratio of SD and SUV value. The %difference (%Diff) of SUV values between the standard images and SS or CBM images was calculated as follows:

$$\%Diff = \frac{SUV_{j-mm} - SUV_{j-mm,ref}}{SUV_{j-mm,ref}} \times 100(\%),$$

where SUV_{j-mm} indicates the SUV values for each sphere in the SS or CBM images and $SUV_{j-mm,ref}$ indicates the SUV values for each sphere in the standard images.

Considering the statistical fluctuations in PET images, $\%Q_H$, $\%N$, and SUV values in both SS and CBM images were calculated by the average values of 10 images (five each of the images acquired in the scan orders of SS → CBM and CBM → SS), while those in standard images were calculated as the average values of five images.

Clinical study

Patients

Whole-body ^{18}F -FDG PET/CT images of 60 patients acquired by both techniques were comparatively analyzed in clinical settings. While 30 patients (male, 12; female, 18; average age, 67.9 ± 12.4 years; average body mass index (BMI), 23.1 ± 3.9 kg/m²; average scan start time, 58.0 ± 3.4 min) were imaged in the SS → CBM order, the remaining 30 patients (male, 14; female, 16; average age, 70.3 ± 11.1 years; average BMI, 23.0 ± 4.1 kg/m²; average scan start time, 58.0 ± 3.3 min) were imaged in the CBM → SS order. All subjects were asked to fast for at least 5 h before imaging. ^{18}F -FDG was intravenously injected with radioactivity of 4.4 MBq/kg (maximum dose, 330 MBq), and PET and CT images were acquired during

free breathing. The image acquisition and reconstruction protocols were same with those described in the phantom study.

This study was approved by the ethics committee of our institution. Written informed consent was obtained from all patients.

Data analysis

Regions of interest of 3-cm diameter were placed on three consecutive coronal slices around the liver section. The ROIs were carefully placed in a uniform area of the liver, apart from the porta hepatis, major vessels, and the subphrenic area, at the same positions in both the SS and CBM images. The mean activity and SD within each ROI was measured. The liver signal-to-noise ratio (SNR_{liver}) was defined as follows:

$$\text{SNR}_{\text{liver}} = \frac{C_{\text{liver}}}{\text{SD}_{\text{liver}}},$$

where C_{liver} and SD_{liver} indicate the mean and SD in the three ROIs.

A total of 36 lesions of 20 patients were quantified through the SUV_{max} . Peak SUV was measured in 19 lesions with the diameters ≥ 12 mm, and the average SUV_{max} of those lesions was 9.0 for SS images reconstructed with TOF. These lesions were located in the salivary glands, thyroid, breast tissue, esophagus, lymph nodes in the neck and chest, and lower abdomen. They were selected because of their relatively low chances of misregistration between CT and PET images due to respiration and peristalsis.

For evaluation of image quality at the end planes, one ROI of 3-cm diameter was placed in the soft tissues of each leg on a transaxial slice and measured for mean activity and SD. The CV at end planes was calculated by the ratio of SD and mean activity.

Statistical analysis

All data are presented as mean \pm SD. In the phantom study, significant differences in $\%Q_{\text{H}}$ and $\%N$ between the two imaging techniques were determined by the Wilcoxon signed-rank test. In the clinical study, significant differences in SNR_{liver}, SUV values, and CV at end planes between the two imaging techniques were determined by the paired t test. $P < 0.05$ was considered as indicating statistical significance. Bland–Altman analysis was used to assess agreement of SUV values between the two imaging techniques.

Results

Phantom study

Regardless of the scan technique, the 10-mm sphere was adjudged to be undetectable upon visual analysis; the visual scores of SS and CBM images reconstructed without the TOF algorithm were 0.93 and 0.7, while those of TOF-reconstructed images were 1.47 and 1.37, respectively. In contrast, all visual scores assigned to spheres of diameters ≥ 13 mm were 2, which indicated that the spheres were obviously detected by both scan techniques. Figure 1 presents representative phantom images acquired by the two techniques in the scan orders of SS \rightarrow CBM and CBM \rightarrow SS and reconstructed with the TOF algorithm. Although the SS and CBM images were of nearly comparable quality, the CBM images exhibited slightly higher background noises, especially in images acquired in the scan order of SS \rightarrow CBM (Fig. 1b).

Table 1 presents $\%Q_{\text{H}}$ values of both sets of images. Because the 10-mm sphere was adjudged to be undetectable, the corresponding values were considered as the reference values. There were no significant differences in $\%Q_{\text{H}}$ values of any of the spheres between the two imaging techniques.

Table 2 presents the $\%N$ values of both sets of images. These values of CBM images tended to be higher than those of SS images, with the difference being significant depending on the size of ROI ($p < 0.05$).

Tables 3 and 4 present the CV and $\%Diff$ values of SUV_{max} and SUV_{peak} , respectively. The average CV and $\%Diff$ for both SUV values in the CBM images tended to be slightly higher than those of SS images.

Clinical study

Figure 2 presents representative images of clinical patients exhibiting the average SNR_{liver} values. Overall, visual analysis revealed slightly higher noises in coronal CBM images than in SS images.

Table 5 presents the values of SNR_{liver}, SUV, and CV at end planes. The SNR_{liver} values of SS images were significantly higher than those of CBM images ($p < 0.01$). While there was no significant difference in SUV_{max} between the two techniques, they exhibited significant differences in terms of SUV_{peak} ($p < 0.05$). The CV at the end planes in CBM images were significantly lower than those in SS images ($p < 0.01$).

Figure 3 presents the results of Bland–Altman analysis for SUV_{max} and SUV_{peak} . In the images reconstructed without TOF, the limits of agreement for SUV_{max} and SUV_{peak} ranged from -1.55 to 2.07 (mean 0.26) and -0.96 to 1.07 (mean 0.05), respectively.

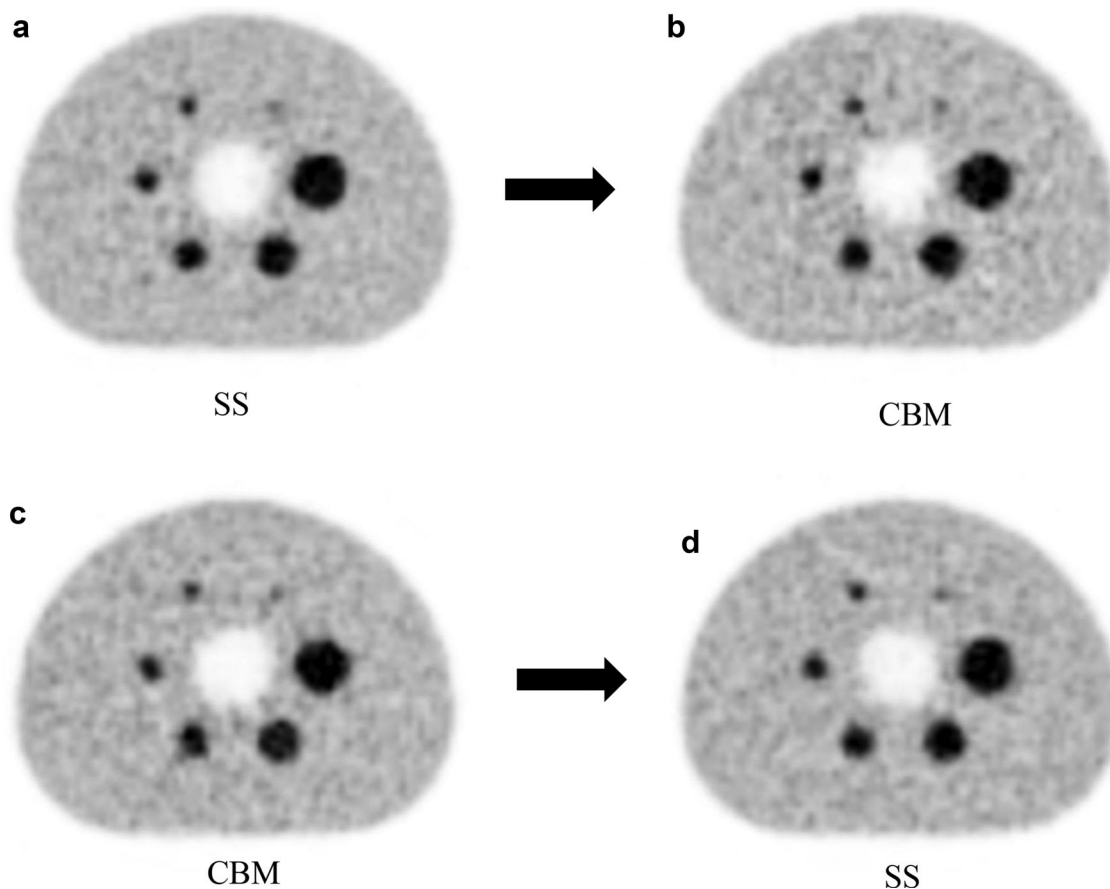


Fig. 1 Representative SS (a, d) and CBM (b, c) images of the phantom. Images were reconstructed using the TOF algorithm. Images in the *upper row* were acquired in the SS → CBM order,

while those in the *lower row* were acquired in the CBM → SS order. SS step-and-shoot, CBM continuous bed motion

Table 1 $%Q_H$ values of the SS and CBM images

Sphere diameter (mm)	Reconstruction algorithm					
	OSEM			TOF–OSEM		
	Imaging technique					
	SS $%Q_H$	CBM	<i>p</i> value	SS $%Q_H$	CBM	<i>p</i> value
10	(20.6 ± 4.2)	(21.5 ± 5.4)	n.s.	(23.3 ± 1.4)	(24.6 ± 3.3)	n.s.
13	43.2 ± 4.5	41.8 ± 2.4		43.7 ± 4.6	41.6 ± 3.9	
17	55.1 ± 1.4	54.6 ± 7.4		55.6 ± 2.1	55.7 ± 6.0	
22	63.9 ± 3.5	65.1 ± 5.3		66.3 ± 4.1	67.0 ± 2.3	
28	71.5 ± 3.6	71.0 ± 3.0		73.3 ± 2.5	72.1 ± 3.6	
37	81.9 ± 2.2	82.4 ± 3.3		83.0 ± 1.9	83.1 ± 1.4	

Since the 10-mm sphere was adjudged to be undetectable on visual analysis, its $%Q_H$ values were considered as the reference values

to 1.75 (mean 0.39), respectively. In the images reconstructed with TOF, the limits of agreement for SUV_{max} and SUV_{peak} ranged from -1.27 to 1.66 (mean 0.20) and -0.89 to 1.55 (mean 0.33), respectively. The lesions that exceeded

the limits of agreement by $+1.96$ SD were scanned in the CBM → SS order. In contrast, the lesions that exhibited SUV_{max} values lower than the limits of agreement by -1.96 SD were scanned in the SS → CBM order.

Table 2 %N values of the SS and CBM images

Sphere diameter (mm)	Reconstruction algorithm					
	OSEM			TOF–OSEM		
	Imaging technique					
	SS %N	CBM	<i>p</i> value	SS %N	CBM	<i>p</i> value
10	9.0 ± 0.6	9.9 ± 1.0	<0.05	7.6 ± 0.5	8.6 ± 0.6	<0.01
13	8.3 ± 0.5	9.0 ± 1.0	<0.05	6.9 ± 0.4	7.8 ± 0.6	<0.01
17	6.8 ± 0.4	7.3 ± 0.9	n.s.	5.5 ± 0.4	6.4 ± 0.6	<0.01
22	5.3 ± 0.4	5.7 ± 0.7	n.s.	4.3 ± 0.4	5.0 ± 0.4	<0.05
28	4.2 ± 0.4	4.6 ± 0.5	n.s.	3.6 ± 0.4	4.0 ± 0.3	<0.05
37	3.3 ± 0.3	3.8 ± 0.3	<0.05	3.0 ± 0.4	3.2 ± 0.3	n.s.

Table 3 CV and %Diff values of SUV_{max} in the SS and CBM images

Sphere diameter (mm)	Reconstruction algorithm							
	OSEM				TOF–OSEM			
	Imaging technique							
	SS		CBM		SS		CBM	
CV (%)	%Diff	CV (%)	%Diff	CV (%)	%Diff	CV (%)	%Diff	
10	(9.8)	(3.8)	(11.3)	(9.1)	(8.6)	(4.0)	(7.4)	(12.0)
13	7.5	3.9	7.3	6.2	7.6	1.6	5.8	4.7
17	4.6	13.0	11.6	9.9	6.2	7.4	10.3	9.9
22	5.2	11.0	5.8	13.7	7.0	15.2	4.9	16.9
28	3.8	17.2	5.5	20.4	4.8	14.7	6.4	19.8
37	3.9	19.9	4.8	25.3	3.6	14.8	4.2	22.5
Average	5.0	13.0	7.0	15.1	5.8	10.8	6.3	14.8

Since the 10-mm sphere was adjudged to be undetectable on visual analysis, its CV and %Diff values were considered as the reference values

Table 4 CV and %Diff values of SUV_{peak} in the SS and CBM images

Sphere diameter (mm)	Reconstruction algorithm							
	OSEM				TOF–OSEM			
	Imaging technique							
	SS		CBM		SS		CBM	
CV (%)	%Diff	CV (%)	%Diff	CV (%)	%Diff	CV (%)	%Diff	
10	–	–	–	–	–	–	–	–
13	6.1	1.8	5.5	1.9	4.4	0.4	3.7	0.0
17	4.0	4.7	8.0	4.5	4.1	1.3	6.1	3.4
22	3.8	–0.1	5.3	0.8	2.5	3.0	3.5	3.0
28	3.0	3.6	3.1	3.1	3.2	3.3	3.2	4.3
37	1.8	7.2	3.4	8.6	1.8	5.3	2.5	7.2
Average	3.8	3.5	5.1	3.7	3.2	2.7	3.8	3.6

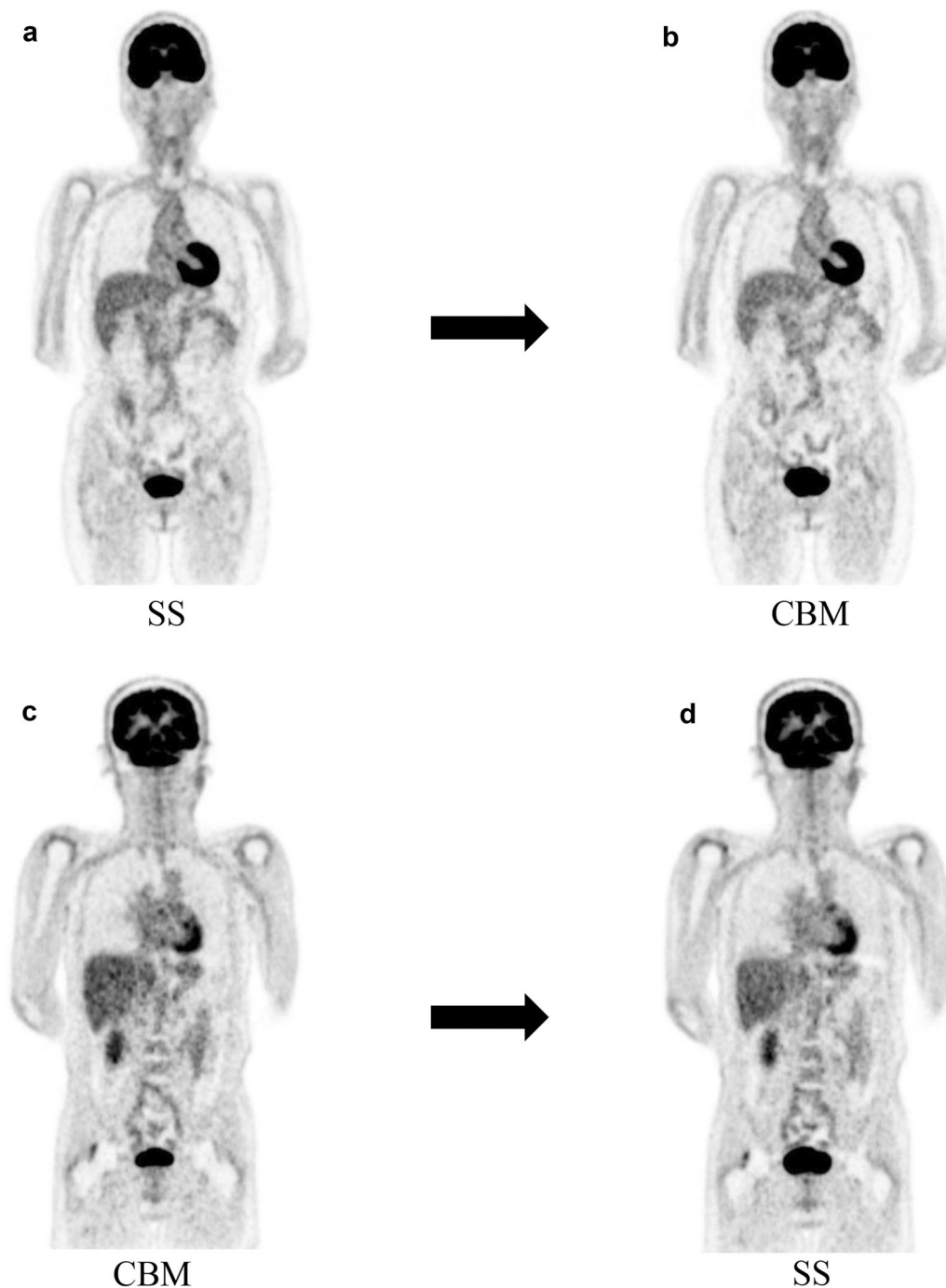


Fig. 2 Representative SS (**a, d**) and CBM (**b, c**) images of clinical patients. Images were reconstructed using the TOF algorithm. Images in the *upper row* were acquired in the SS → CBM order. The SNR_{liver} values of the SS (**a**) and CBM (**b**) images were 9.6 and 8.4,

respectively. Images in the *lower row* were acquired in the CBM → SS order. The SNR_{liver} values of the CBM (**c**) and SS (**d**) images were 8.2 and 9.6, respectively. *SS* step-and-shoot, *CBM* continuous bed motion, *SNR_{liver}* liver signal-to-noise ratio

Discussion

We investigated the differences in the quality of phantom and clinical images acquired using the SS and CBM techniques with approximately the same acquisition duration.

In the phantom study, there were no significant differences in $\%Q_H$ values of any of the spheres between the two imaging techniques, which corresponded to the findings of a previous study [14]. The present $\%Q_H$ values were, however, lower than those reported in a previous study [14], because of the differences in reconstruction

Table 5 SNR_{liver}, SUV, and CV at end planes in the SS and CBM images of the clinical patients

	Reconstruction algorithm					
	OSEM			TOF-OSEM		
	Imaging technique					
	SS	CBM	<i>p</i> value	SS	CBM	<i>p</i> value
SNR _{liver}	9.3 ± 1.7	8.5 ± 1.7	<0.01	9.6 ± 1.7	8.7 ± 1.6	<0.01
SUV _{max}	6.5 ± 4.8	6.2 ± 4.5	n.s.	6.5 ± 4.7	6.3 ± 4.4	n.s.
SUV _{peak}	6.9 ± 4.6	6.5 ± 4.2	<0.05	6.9 ± 4.6	6.5 ± 4.1	<0.05
CV at end planes	99.6 ± 25.4	58.1 ± 14.7	<0.01	98.2 ± 25.7	54.8 ± 12.1	<0.01

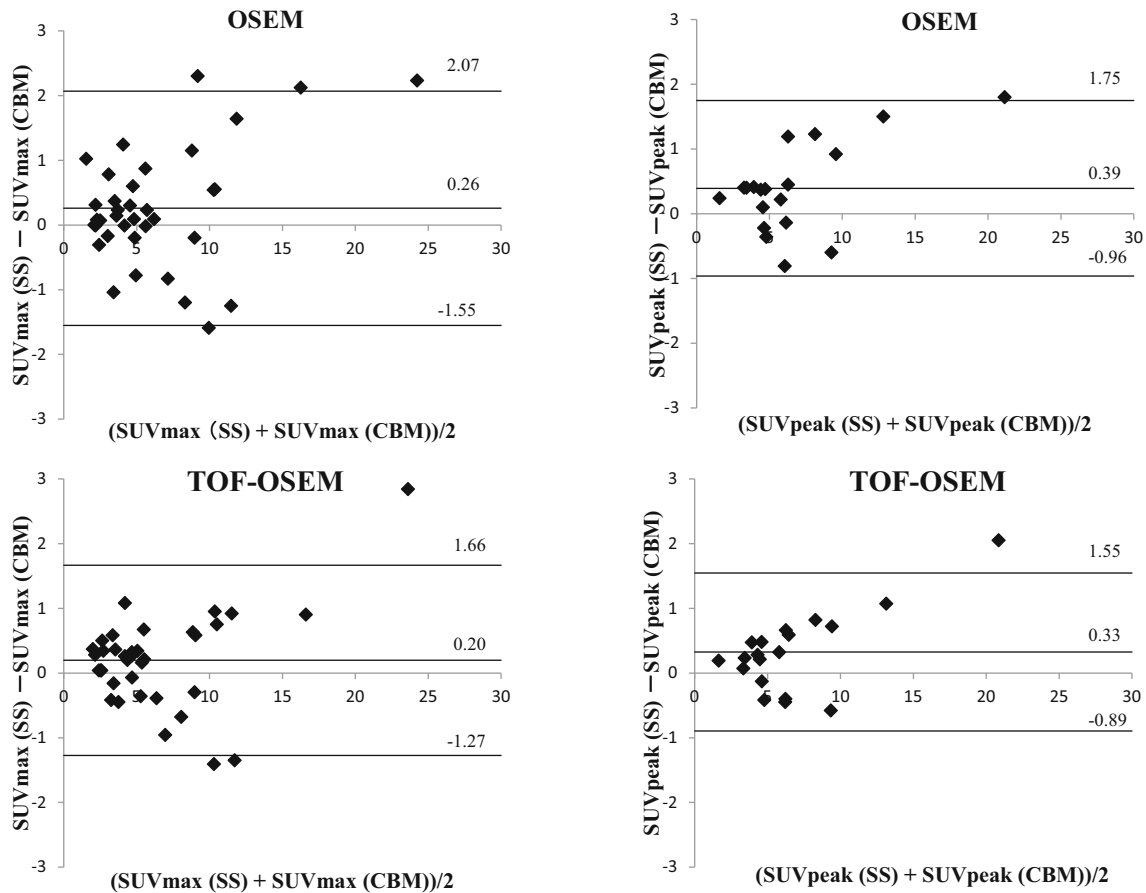


Fig. 3 Bland–Altman analysis for SUV_{max} (left) and SUV_{peak} (right). These lesions were reconstructed without (top) and with TOF (bottom)

parameters, especially a point spread function technique which produces inaccurate quantitative values due to the Gibbs artifact was not used in this study, although the technique improves lesion detectability [16, 17].

However, the %N values of the CBM technique were significantly higher than those of the SS technique, which corresponded with the findings of a previous study [14]. In the clinical study, the SNR_{liver} values of CBM images were significantly lower than those of SS images. These results indicate that the image uniformity of the SS technique is better than that of the CBM technique. The relatively low

uniformity observed in CBM image is possibly attributable to the following reasons. First, in the PET/CT scanner used in this study, the CBM technique requires 50% overscan to obtain a uniform profile for the entire scan length and ensure equivalent image quality as that obtained in the SS mode [9]. This overscan leads to improved image quality at the end planes in the axial FOV, as demonstrated in the clinical study; however, some of the overscan data are discarded, and therefore, do not contribute to the quality of reconstructed images. The CBM technique requires a redundant scan range over the SS technique, which causes

its image uniformity at the center plane to be lower than that of the SS technique, despite the acquisition duration and scan range being the same. Second, in this study, the phantom was imaged with overlapping regions, including low-sensitivity areas in the axial FOV. The scanner has an overlap region of 43%, which is adequate for obtaining SS images of appropriate quality. If the phantom had been scanned with the center of the detector having access to the most sensitive area, the resultant SS images would have exhibited better $\%Q_H$ and $\%N$ values. Third, in the SS mode, the table remains stationary during image acquisition. In contrast, the table is moved continuously during imaging in the CBM mode, which might lead to a slight axial blurring [9]. Fourth, CBM data are large-sized 3D volumetric data covering the entire axial scan range. Consequently, they are divided into sub-volumes for image reconstruction as SS data [8, 9], which could result in additional noise included in the images. In addition, the challenges of the normalization technique, random smoothing, and/or Fourier rebinning process might result in increased noise, as mentioned by a previous report [14].

The $\%N$ value is important for the detection of hot sphere detectability [15]. Although the relatively high $\%N$ had no influence on the visual scores of the hot spheres in this study, further investigation is required to determine whether the decrease in uniformity in CBM images influences the findings of visual assessment in clinical settings, especially in case of small lesions surrounded by high-radioactivity areas such as liver tissues.

With respect to SUV values, the CV and $\%Diff$ of SUV values in CBM images tended to be slightly higher than those of SS images. However, there was no significant difference in SUV_{max} between the two techniques in the clinical study, as reported in previous studies [12, 13]. Since those differences were subtle, they might be negligible in clinical settings. Nevertheless, the CBM and SS methods differed significantly in terms of SUV_{peak} . We considered the possibility that the statistical difference was accidentally caused by the differences in uptake time depending on the scan order because most of the lesions (13 of 19) that were quantified by SUV_{peak} were acquired by the CBM \rightarrow SS order. The SUV_{peak} of SS images were, therefore, significantly higher than that of CBM images. However, in Bland–Altman analysis, the mean SUV_{peak} differences were close to 0, and the values of almost all the lesions were within the limits of agreement, although the limits of agreement depends on the variability of measurements, which implied that the SS and CBM techniques provided comparable values of SUV_{peak} . This result demonstrates not only the reliability of the CBM technique for quantitative analyses but also its feasibility in terms of repeatability, reproducibility, and SUV harmonization for clinical management of patients and multicenter studies with different PET/CT scanners [18, 19]. Recent studies have

proposed quantitative methods for assessment of intratumoral heterogeneity, such as texture and fractal analyses [20, 21]. Future studies need to investigate whether the SS and CBM techniques produce comparable results in such analyses.

The 10-mm sphere in the phantom was undetectable by either technique, and the SNRLiver values did not achieve the recommended values (>10) of the Japanese guideline [15]. In this study, the acquisition times for both techniques were relatively short in consideration of the patient burden and body motion. However, longer acquisition times are desirable for clinical application.

Despite the acquisition times being the same, the CBM technique exhibited slightly lesser uniformity in the center plane than the SS technique. Nevertheless, the CBM technique offers great advantages in terms of flexible acquisition planning and patient comfort during imaging. The flexibility of acquisition enables the selection of the optimal scan ranges at the beginning and end planes and the configuration of multiple areas with desired bed speed, depending on the organ and disease. The complex imaging protocol enables easy acquisition of high-resolution and gated images. These advantages translate into reduced scan time, patient motion, and radiation exposure during CT [5]. With respect to patient comfort, the CBM technique is preferred over the SS technique because of being less abrupt in motion, more silent, and more relaxing [13]. Since the CBM and SS methods both have several advantages and disadvantages, selection of the optimal scan technique must be made carefully.

There are some limitations in this study. Although the present study employed a single table speed, the differences in image quality between the two techniques might be influenced by the table speed [12]. These differences might be influenced by the scan range as well [22].

Conclusions

The CBM technique exhibited slightly lesser uniformity in the center plane than the SS technique. Additionally, in the phantom study, the CV and $\%Diff$ of SUV values in CBM images tended to be slightly higher than those of SS images. However, since these differences were subtle, they might be negligible in clinical settings.

References

1. Dahlbom M, Reed J, Young J. Implementation of true continuous bed motion in 2-D and 3-D whole-body PET scanning. *IEEE Trans Nucl Sci.* 2001;48:1465–9.
2. Kitamura K, Tanaka K, Sato T. Implementation of continuous 3D whole-body PET scanning using on-the-fly Fourier rebinning. *Phys Med Biol.* 2002;47:2705–12.

3. Burbar Z, Michel C, Townsend D, Jakoby B, Sibomana M, Kehren F, et al. Continuous bed motion data processing for a high resolution LSO PET/CT scanner. *IEEE Nucl Sci Symp Conf Rec.* 2005;4:2046–8.
4. Brasse D, Newport D, Carney JP, Yap JT, Reynolds C, Reed J, et al. Continuous bed motion acquisition on a whole body combined PET/CT system. *IEEE Nucl Sci Symp Conf Rec.* 2002;2:951–5.
5. Acuff S, Osborne D. Clinical workflow considerations for implementation of continuous-bed-motion PET/CT. *J Nucl Med Technol.* 2016;44:55–8.
6. Dahlbom M, Yu DC, Cherry SR, Chatziioannou A, Hoffman EJ. Methods for improving image quality in whole body PET scanning. *IEEE Trans Nucl Sci.* 1992;39:1079–83.
7. Dahlbom M, Cutler PD, Digby WM, Luk WK, Reed J. Characterization of sampling schemes for whole body PET imaging. *IEEE Trans Nucl Sci.* 1994;41:1571–6.
8. Townsend D, Reed J, Newport D, Carney JPI, Tolbert S, Newby D, et al. Continuous bed motion acquisition for an LSO PET/CT scanner. *IEEE Nucl Sci Symp Conf Rec.* 2004;4:2383–7.
9. Panin VY, Smith AM, Hu J, Kehren F, Casey ME. Continuous bed motion on clinical scanner: design, data correction, and reconstruction. *Phys Med Biol.* 2014;59:6153–74.
10. Braun H, Ziegler S, Lentschig MG, Quick HH. Implementation and performance evaluation of simultaneous PET/MR whole-body imaging with continuous table motion. *J Nucl Med.* 2014;55:161–8.
11. Braun H, Ziegler S, Paulus DH, Quick H. Hybrid PET/MRI imaging with continuous table motion. *Med Phys.* 2012;39:2735–45.
12. Osborne DR, Acuff S, Cruise S, Syed M, Neveu M, Stuckey A, et al. Quantitative and qualitative comparison of continuous bed motion and traditional step and shoot PET/CT. *Am J Nucl Med Mol Imaging.* 2014;5:56–64.
13. Schatka I, Weiberg D, Reichelt S, Owsianski-Hille N, Derlin T, Berding G, et al. A randomized, double-blind, crossover comparison of novel continuous bed motion versus traditional bed position whole-body PET/CT imaging. *Eur J Nucl Med Mol Imaging.* 2016;43:711–7.
14. Rausch I, Cal-Gonzalez J, Dapra D, Gallowitsch HJ, Lind P, Beyer T, et al. Performance evaluation of the Biograph mCT Flow PET/CT system according to the NEMA NU2-2012 standard. *EJNMMI Phys.* 2015;2:26.
15. Fukukita H, Suzuki K, Matsumoto K, Terauchi T, Daisaki H, Ikari Y, et al. Japanese guideline for the oncology FDG-PET/CT data acquisition protocol: synopsis of Version 2.0. *Ann Nucl Med.* 2014;28:693–705.
16. Tong S, Alessio AM, Thielemans K, Stearns C, Ross S, Kinahan PE. Properties and mitigation of edge artifacts in PSF-based PET reconstruction. *IEEE Trans Nucl Sci.* 2011;58:2264–75.
17. Akamatsu G, Mitsumoto K, Taniguchi T, Tsutsui Y, Baba S, Sasaki M. Influences of point-spread function and time-of-flight reconstructions on standardized uptake value of lymph node metastases in FDG-PET. *Eur J Radiol.* 2014;83:226–30.
18. Boellaard R, Delgado-Bolton R, Oyen WJ, Giammarile F, Tatsch K, Eschner W, et al. FDG PET/CT: EANM procedure guidelines for tumour imaging: version 2.0. *Eur J Nucl Med Mol Imaging.* 2015;42:328–54.
19. Lasnon C, Desmots C, Quak E, Gervais R, Do P, Dubos-Arvis C, et al. Harmonizing SUVs in multicentre trials when using different generation PET systems: prospective validation in non-small cell lung cancer patients. *Eur J Nucl Med Mol Imaging.* 2013;40:985–96.
20. Chicklore S, Goh V, Siddique M, Roy A, Marsden PK, Cook GJ. Quantifying tumour heterogeneity in 18F-FDG PET/CT imaging by texture analysis. *Eur J Nucl Med Mol Imaging.* 2013;40:133–40.
21. Takeshita T, Morita K, Tsutsui Y, Kidera D, Mikasa S, Mae-batake A, et al. The influence of respiratory motion on the cumulative SUV-volume histogram and fractal analyses of intratumoral heterogeneity in PET/CT imaging. *Ann Nucl Med.* 2016;30:393–9.
22. Everding M, Emery D, Mawlawi O, Millican-Campbell R, Palendat T, Pan T, et al. Impact of continuous bed motion (CBM) PET/CT scanners on clinical operation (abstract). *J Nucl Med.* 2014;55(Suppl 1):2511.